Constraining the Ages of Late Devonian Extinction Events in the Central Asian Orogenic Belt (CAOB): U-Pb Geochronology and Igneous Petrology

Cameron Batchelor

Department of Geology: Appalachian State University

Advisers:

Dr. Sarah K. Carmichael

Signature: _____Date:_____

Dr. Johnny A. Waters

Signature: _____Date:_____

Table of Contents

Abstract

The Late Devonian was a time of drastic changes in climate and biodiversity. Two of the top six most devastating extinction events occurred during the Late Devonian, although the reasons for these extinction events remains unknown. More than 96% of studies on these Late Devonian extinction intervals have been conducted on continental margins or in epicontinental basins, with 77% on the Euramerican continent alone. There are very few studies of these Late Devonian mass extinction events in a paleogeographically different region: the open ocean island arc systems in the Central Asian Orogenic Belt (CAOB). Sedimentary rocks and lava flows were collected from the Samnuuruul Formation in western Mongolia during fieldwork in 2014 for U-Pb geochronology analyses of zircons. The chemical-abrasion thermal ionization mass spectrometer (CA-TIMS) technique was used to analyze these zircons. Age results for sample SAM 4-8 show a final age of 375.81 +/- 1.20 Ma, and sample MBL 7 show a final age of 376.75 +/- 0.90 Ma. These ages indicate that both samples have a Frasnian age. Until now, the only age constraints that existed for these sections were based on limited biostratigraphy; this is the first study to radiometrically date Late Devonian rocks from western Mongolia. This study will further constrain the location of Late Devonian extinction intervals in a section that was once part of the CAOB, therefore opening doors to new research opportunities of these events in a geographically different region than what has been studied before.

Acknowledgments and Dedication

This thesis is dedicated to my two research advisers, Dr. Sarah Carmichael and Dr. Johnny Waters, who taught me adventure and wonder is closer than arms reach when it comes to research in geology and to never stop exploring. To the professors, graduate students, and undergraduate students at the University of North Carolina at Chapel Hill (Dr. Drew Coleman, Ryan Frazer, Dr. Ryan Mills, Connor Lawrence, Tom Chapman, Sean Gaynor, Kyle Bullins, Mandy Suttner) for all of their help in the lab the past three summers conducting geochemistry and geochronology research. To my two loving parents, mom and dad, who taught me hard work can get you anywhere in life. To my best friend and sister, Chase Batchelor, who first showed me the footsteps that led to my path in geology. To my grandparents, Grandpa, Nana, Mamaw and Papaw, and my aunt Marcie and aunt Beverly who are my biggest support team. To all my friends who stayed my friend through college, even though I was a busy geology major (shout out to you Lena Lendermann, Christine Lee, Whitney Wright, Doug Mulford, Kelsey Wayne, Kelli Straka, Colleen McKearney, Meredith Hicks, Alexis Abraham, Savannah Idol, and Candace Bunch). To my high school AP Environmental Science teacher, Dr. Dennis DuBay, who inspired my first passion to discover Earth's mysteries. To the International Geoscience Programme Projects 596 & 580 for helping my time spent in both Mongolia and Belgium conducting fieldwork become rewarding experiences of which I will never forget. And finally to all of the faculty and staff part of the Appalachian State Department of Geology-thank you for making the past three and a half years the best years of my life yet and for providing me with the absolute best education in the field of geology.

Here is to a future in a Masters, and eventually a Ph.D. - and to *never stop exploring.*

Chapter 1. Introduction

Mass extinction is described as "any substantial loss of more than one geographically widespread higher taxon during a relatively short interval of geologic time, resulting in a temporary decline in their standing diversity," (Sepkoski, 1986). Even though they are detrimental to many species, the largest mass extinctions produce major restructuring of the biosphere where minor groups can grow and diversify (Sepkoski, 1986). They are important for the evolution of life throughout Earth history.

The Late Devonian

The Devonian period (419- 358 Ma) in the Middle Paleozoic was a time characterized by warm climate and widespread tectonic activity, with diverse life in the ocean and on land (McGhee, 2013). Two supercontinents, Laurentia and Gondwana, were beginning to collide resulting in the formation of a supercontinent at mid to low latitudes (Scotese and McKerrow, 1990). Marine fauna such as brachiopods, trilobites, rugose corals, stromatoporoid corals, calcareous forminifera, marine phytoplankton, and biohermal reefs flourished during the Devonian (Schindler, 1993). There was also a distinct decline in jawless fish and rise in jawed fish during the Middle Devonian (Klug et al., 2010). On land, there was a large increase in plant life with the evolution of both tree and seed plants (Berner and Kothavala, 2001), which is attributed to the first soil formation and resulting nutrient flux into oceans (Algeo et al., 1995; Algeo and Scheckler, 2010). In the Late Devonian, multi-storied forests began to develop, along with the first appearance of the tetrapod in the Fammennian (Niedźwiedzki et al., 2010).

The Late Devonian (372-359 Ma) was bracketed by two catastrophic mass extinction events: the Kellwasser Event at the Frasnian-Fammenian (F-F) boundary and the Hangenberg

Event at the Devonian-Carboniferous (D-C) boundary. The Kellwasser Event occurred at about 372 Ma, and was characterized by the extinction of ~80% marine fauna (McGhee et al., 2013). The Hangenberg Event occurred at ~359 Ma, and involved long-term losses in diversity, primarily of pelagic marine communities (Kaiser et al., 2015). A recent revised taxonomic severity ranking has the Hangenberg Event and the Kellwasser Event rated in the top five most devastating biologic crises in history (McGhee, 2013).

In contrast to the other major mass extinctions of the Phanerozoic than can be attributed to a single event, the mass extinction events in the Late Devonian are suggested to be a result of a series of 'extinction pulses' occurring over several million years (Racki, 2005). Numerous hypotheses for the mechanisms triggering these extinction events include meteorite impacts (Caplan and Bustin, 1999), volcanism (Bond and Wignall, 2014), and astronomical climate forcing (De Vleeschouwer et al., 2013).

The Frasnian-Famennian extinction is stratigraphically associated with a pair of ocean anoxia events (the Upper and Lower Kellwasser Anoxia Events), which are suggested to have been triggered by sea level oscillations, tectonic forcing, and/or ocean stratification (Bond et al., 2004; Chen et al., 2013; Joachimski and Buggisch, 1993; McGhee, 1996; Wang et al., 1996) . The Hangenberg Event is also associated with ocean anoxia, suggested to have resulted from global cooling and gradual glaciations at the end of the Famennian (Brezinski et al., 2010; Brezinski et al., 2009; Cole et al., 2015; Isaacson et al., 2008; Myrow et al., 2014). These specific mechanisms, however, prove to be contradictory because they are solely reliant on factors such as local topography and tectonic activity (Racki, 2005).

Black shale deposits have been found representing these Late Devonian anoxia events in areas such as Alberta (Caplan and Bustin, 1998), epicontinental basins located in both the central and

eastern United States, (Formolo et al., 2014; Perkins et al., 2008; Rimmer, 2004), Vietnam (Komatsu et al., 2014), Poland (Kumpan et al., 2014; Matyja et al., 2015), the Czech Republic (Kumpan et al., 2013), Germany (Myrow et al., 2014), and others in France and Belgium (Girard et al., 2014; Kumpan et al., 2014; Mottequin et al., 2014). It has been suggested that these black shales are indicative of eutrophication induced by upwelling (Algeo and Scheckler, 1998; Caplan et al., 1996; Cramer et al., 2008; Murphy et al., 2000). Other possible mechanisms for this marine anoxia also include eutrophication (Averbuch et al., 2005; Caplan and Bustin, 1998; Carmichael et al., 2014), as well as forest fires and soil erosion (Kaiho et al., 2013).

Black shale deposits, however, are not representative of the F-F and D-C boundaries at every locality, as no black shale has been correlated with the Kellwasser or Hangenberg Events in southern Belgium (Azmy et al., 2009), southeastern Morocco (Kaiser et al., 2011), southwestern Thailand (Königshof et al., 2012), Poland (Matyja et al., 2015), Canada (Bond et al., 2013) and the CAOB (Carmichael et al., 2015; Carmichael et al., 2014; Suttner et al., 2014).

Most studies of these Late Devonian mass extinction events have been conducted on continental margins or epicontinental basins in both North America and Europe (see summary in Carmichael et al. (2015)), which may be leading to a tectonic megabias (Carmichael and Waters, 2015). Recent studies by Carmichael et al. (2014), Carmichael et al. (2015), Suttner et al. (2014), and Kido et al. (2013) are the first to examine these mass extinction events from a paleogeographically different tectonic setting: the Central Asian Orogenic Belt (CAOB) (Figure 1A) During the Devonian, the CAOB consisted of clusters of island arcs and microcontinents (Choulet et al., 2012; Xiao et al., 2010), representing an open ocean system. By studying Late Devonian units in a different paleogeographic region, factors associated with the climate

instability of this time that may have triggered these mass extinction events can be better understood.

Tectonic Setting

The Central Asian Orogenic Belt (CAOB), also referred to as the Altaid Collage, consists of several ribbon-like micro-continents, magmatic arcs, and accretionary wedges with ophiolitic fragments that merged together during the Paleozoic (Xiao et al., 2010) (Figure 1A). This segment of largely juvenile continental crust stretches from Kazakhstan in the west to Siberia in the east (Xiao et al., 2010). As proposed by Choulet et al. (2012), the CAOB experienced two major tectonic-magmatic episodes during its Paleozoic evolution; the first was Ordovician-Silurian subduction/accretion that generated the basement rock, followed by a Devonian-Carboniferous subduction that formed the accretionary complexes and molasse-filled foredeeps (Choulet et al., 2012; Sengör et al., 1993).

The Baruunhuurai Terrane in western Mongolia is part of the East Junggar arc (Figure 1B) and contains sedimentary rocks deposited in an open oceanic setting during the Late Devonian that were once part of the CAOB (Kido et al., 2013). Within the Baruunhuurai Terrane, the Samnuuruul Formation is thought to contain the F-F and D-C boundary, with the only age constraints of the section based on limited biostratigraphy (Figure 2) (Kido et al., 2013). The section is unique for not only its exceptional preservation of plant, fish, and miscellaneous fossils that were present during the Devonian, but also for its structural complexity (Kido et al., 2013).

Preliminary observations during fieldwork conducted in 2014 indicated these sections were Frasnian instead of Famennian in age (Bernard Mottequin and Edouard Poty, personal

communication). In order to better constrain the age of the units, samples were taken from the sedimentary and volcanic rocks of the Baruunhuurai Terrane for U-Pb geochronology and petrographic analysis. The research presented in this thesis will provide the first radiometric dates of Late Devonian rocks in western Mongolia and will help constrain both the F-F and D-C boundaries within these sections.

Chapter 2. Principles of U-Th-Pb geochronology

Background

U-Th-Pb geochronology is possible from the decay of multiple parent isotopes to different stable isotopes of Pb, each with different half-lives (Schoene, 2014). All Pb in a zircon crystal is a direct decay product of U and Th, therefore making age results contingent on specific values of the daughter products (Nebel et al., 2011). Zircon is one of the most popular mineral for geochronometry because of an usually high abundance of U-bearing minerals in most rock types, and the ability for zircons able to resist both chemical and physical weathering (Schoene, 2014).

U and Th are members of the actinide series of elements in which the 5f orbitals are progressively filled with electrons (Faure, 1998). Due to similar electron configurations, Th (Z=90) and U (Z=92) have similar chemical properties and since their ions have similar radii, the two elements can readily substitute for each other (Faure, 1998). The element Pb has four naturally occurring stable isotopes, of which three have a radiogenic component produced through the independent decay of:

$$^{238}_{92}U \rightarrow {}^{206}_{82}Pb + 8\ {}^{4}_{2}He + 6\beta^{-} + Q \quad \textbf{(1)}$$

$$^{235}_{92}U \rightarrow {}^{207}_{82}Pb + 7\ {}^{4}_{2}He + 4\beta^{-} + Q \quad \textbf{(2)}$$

$$^{232}_{90}Th \rightarrow {}^{208}_{82}Pb + 6\ {}^{4}_{2}He + 4\beta^{-} + Q \quad \textbf{(3)}$$

Q represents the sum of the decay energies of the entire series in units of million electron volts (Schoene, 2014).

Secular equilibrium occurs when the decay rates of intermediate daughters reach equilibrium with those of their respective parents (Schoene, 2014) When secular equilibrium is established, exactly one Pb daughter is produced for every one U parent decayed, and therefore

the ratio of Pb to U can be easily measured to calculate an age (Schoene, 2014). For secular equilibrium to be established, the half-lives of parents need to span much longer than respective daughters in order to eventually reach equilibrium, as the U to Pb decay chain is not direct since the respective daughters have several intermediate daughter products (Figure 3). The half-lives of ^{238}U, ^{235}U, and ^{232}Th do span much longer than respective Pb daughters, therefore secular equilibrium can be established for each isotope and represents a key component in the success of zircon geochronometry (Schoene, 2014).

For a closed system, equilibrium will be achieved when the decay chain of the parent is proportional to the longest half-life of the intermediate daughter (Schoene, 2014). For an accurate age of a zircon to be obtained, the crystal cannot be disturbed during formation or partial melting and must stay in secular equilibrium (Faure, 1998). Open system behavior occurs when a crystal is compromised and does not remain in secular equilibrium (Faure, 1998; Schoene, 2014) and methods such as the chemical abrasion thermal ionization mass spectrometer (CA-TIMS) technique have been developed to correct for zircons that experience this kind of behavior (Mattinson, 2005; McLean et al., 2011; Schmitz and Schoene, 2007).

For age calculations of zircons, it is essential to use a stable isotope of the daughter element to be chosen for normalization (Schoene, 2014). The stable isotope used in this study was ^{204}Pb as it is the only non-radiogenic isotope of Pb. Normalization is important when calculating age because it allows for the absolute concentration of both U and Pb to be based only off a ratio and not the specific amount of concentrations, therefore allowing for less error (Schoene, 2014). Age equations used include:

$$\frac{^{206}Pb}{^{204}Pb} = (\frac{^{206}Pb}{^{204}Pb})_0 + (\frac{^{238}U}{^{204}Pb})(e^{\lambda_{238}t} - 1) \textbf{ (4)}$$

$$\frac{^{207}Pb}{^{204}Pb} = (\frac{^{207}Pb}{^{204}Pb})_0 + (\frac{^{235}U}{^{204}Pb})(e^{\lambda_{235}t} - 1) \textbf{ (5)}$$

$$\frac{^{208}Pb}{^{204}Pb} = (\frac{^{208}Pb}{^{204}Pb})_0 + (\frac{^{232}Th}{^{204}Pb})(e^{\lambda_{232}t} - 1) \quad \textbf{(6)}$$

The subscript 0 following certain ratios represent the isotopic composition when a system is closed, t is the time since the system closed, and λ_{238}, λ_{235}, and λ_{232} are the decay constants of ^{238}U, ^{235}U, and ^{232}Th (Faure, 1998; Schoene, 2014). Initial Pb (Pb_0) is called common lead, which is initial Pb plus Pb from the sample blank and potential contamination (non-radiogenic Pb introduced during laboratory work or naturally prior to sampling). With these three equations, accurate ages of zircons can be interpreted with proper error analysis.

Chemical abrasion-thermal ionization mass spectrometry (CA-TIMS)

Zircons can experience partially open system behavior that causes Pb loss, which can significantly affect the accuracy of age determinations (Schoene et al., 2010). A variety of methods have been developed to correct for errors associated with non-perfect zircons that have been affected by partially open system behavior; these include air abrasion (Krogh, 1982), graphical concordia diagrams (Wetherill, 1956), and specific grain selection techniques (Mundil et al., 2004). In this study, the CA-TIMS method developed by Mattinson (2005) was used to analyze all zircons. This method combines high-temperature annealing with multi-step partial dissolution analysis (PDA) to remove zones of zircon grains that have lost Pb (Mattinson, 2005). Initial annealing steps are used to strengthen zircon grains prior to PDA steps, so the entire zircon grain does not dissolve, just the weaker outer zones (Mattinson, 2005). Partial dissolution of zircon grains is an effective way to remove zones within a zircon with highest U+Th+ trace-element concentrations from Pb loss since these zones are commonly located on the outermost zones of a zircon due to magmatic zoning (Mattinson, 2005). Therefore, combining both annealing and PDA steps of the CA-TIMS method effectively removes zircon zones with high

Pb loss allowing for ages that are calculated from more accurate, internal zones (Mattinson, 2005).

Chapter 3. Field Site

In August 2014, members of IGCP Projects 580 & 596 collected 69 samples at four different locations within the Samnuuruul Formation in western Mongolia (Figure 4). The Buduun Khargait River Locality (aka "War Monument Locality"), located at 45°17'06"; 90°57'31," ranges from 250-450 meters thick and has been subjected to extreme folding, faulting, and fracturing from joint sets. All units in this section were originally measured bed-by-bed into four sections in 2012 (Kido et al., 2013). Additional field work was done in 2014 (this study) where beds were re-measured and additional samples were collected. The Buduun Khargait River of the Samnuuruul Formation is split into sections 2, 3, and 4. Units 2 and 3 predominantly consist of dark gray, green, to gray calcareous siltstone, sandstone, interbedded limestone and sandy shale. Large spheres (20cm-60cm thick) of dark colored material were found in the lower part of unit 2 and were originally interpreted to be microbiolite deposits although their exact formation mechanism remains unknown. Unit 4 is characterized by a series of coarse sandstones and conglomerates with interbedded siltstones and shales that contain plant debris. The base of Unit 4 was originally mapped with a marine black shale unit and a soil horizon of coal, hypothesized to represent the Hangenberg Event and the D-C boundary (Kido et al., 2013). Re-mapping in 2014, however, indicated that the bed originally interpreted to be a black shale was actually a soil horizon, and brachiopod fauna in Unit 4 were reinterpreted as Frasnian rather than Famennian (Bernard Mottequin and Edouard Poty, personal communication,). Samples collected from the Buduun Khargait River include: 11 shales, 24 coarse sandstones/conglomerates, 1 microbialite, and 1 chert horizon. Of these, 13 were selected for zircon dating (Table 1).

The second formation, near Kushuut-Shiveet River Locality (aka “Car Wreck Locality,”) located at 45°16’18”; 90°03’20 consists of fossil-rich siltstones that are correlated with Unit 3 in the Buduun Khargait River Locality. Samples collected from this location were prefixed with the abbreviation of “HS” and include: 1 fossiliferous sandstone, 2 conglomerates, 4 pillow basalts, and 2 black shale samples (Table 1). A mix of the conglomerates and mafic pillow basalts were collected for zircon dating.

The third locality was located directly at the Shiveet Mountain Locality (aka “Mongolian Border Locality”), located at 45°05’02”; 91°34’13", and contains low-grade metamorphic sediments, with a thick interval of highly fossiliferous slates. Fossils found in the slate layers consist of brachiopods, rugose corals, trilobites, bryozoan colonies, and crinoid crowns. In this locality there is an evident transition from a Devonian marine to Carboniferous terrestrial paleoenvironment. Samples collected from this location have a prefix of MBL and include: 1 pillow basalt sample, 1 sandstone sample, and 1 basalt dike sample (Table 1).

The fourth locality at the base of the Samnuuruul Formation (aka "Lost Bentonite Canyon") consisted of a colorful layer of fine grained sandstone, mudstone, phyllite, and bentonite. A sample of bentonite was collected from the “Bentonite Locality” for zircon dating.

Chapter 4. Laboratory Methods

Zircon geochronology: CA-TIMS Method

All zircon geochronology analyses were conducted at the University of North Carolina at Chapel Hill. Preliminary steps for the CA-TIMS method include zircon samples being prepared with mineral separation and purification techniques. Zircons were extracted from samples by standard crushing methods using both a jaw crusher and disk mill, and separated using gravimetric techniques including a water table, Franz-magnetic separator, and heavy liquids (Tetrabromide-TBE). Zircons were then hand-picked using a binocular microscope.
After sorting, zircons were annealed in a quartz crucible at 900˚ C for 48 hours. After annealing, grains were placed in a hexagon-cap Savillex® Teflon bomb and chemically abraded with a mixture of 500 mL of hydrogen fluoride (HF) and 500 mL of nitric acid (HNO_3) for 12-16 hours at 180°C. This initial chemical abrasion technique is used to dissolve all weak zircons that have suffered extreme Pb loss and would not be fit for analysis. Zircons that remain after chemical abrasion were ultrasonically cleaned with a mixture of deionized (DI) water and hydrochloric acid (HCl). Each zircon grain was then assigned an individual fraction number. Five individual zircons were chosen for dating each rock sample. Each individual zircon was then placed in a separate beaker and rinsed three times with 500 mL of HNO_3 and 450 mL of DI water. After this, each zircon was spiked with 0.006-0.010 mL of ^{205}Pb-^{233}U-^{236}U tracer and 100 mL of HF. Then each microcap was placed in a hexagon-cap Savillex® Teflon bomb at 220°C for 48-72 hours to fully dissolve.

Once dissolved, each zircon fraction was dried on a hot plate set at 110°C for 3-5 hours and then was converted into chloride salt for preparation of column chemistry to leach out all U and Pb. To convert to chloride salt, 100 mL of 6N HCl were added to each microcap and then

placed into hexagon-cap Savillex® Teflon bomb at 180°C for 12 hours. After fully dissolved, zircon fractions were then dried down into chloride salt on a hotplate set at 110°C for 3-5 hours. When finally converted to a chloride salt, 50 µl of 3N HCl was added to each microcap for preparation of column chemistry.

For column chemistry, 15 µl of clean resin were added to each of five individual columns. Resin was cleaned and pre-conditioned by adding 500 mL of 6N HCl three times, followed by 250 mL of DI water and 250 mL of 6N HCl. Samples were then loaded into each column in a prepared solution of 3N HCl and were pre-conditioned with four rinses of 50 µl 3N HCl prior to Pb or U collection. Once pre-conditioned, U and Pb were extracted from the sample using different techniques. Lead was eluted by adding 63 µl of 6N HCl into each column that dripped into separate 7 mL beakers. Uranium was eluted by adding 25 µl of DI water into each column that dripped into separate 5 mL beakers. After Pb and U collection, approximately 15 µl of phosphoric acid (H_3PO_4) was added to each beaker and both were dried down on a hot plate set at 110˚C until a final bead was ready for loading (about 2 hours).

All analyses were conducted on a Sector 54 Thermal Ionization Mass Spectrometer (TIMS) at the University of North Carolina at Chapel Hill. Uranium was run on a Re single-ribbon filament as an oxide after loading in silica gel. Lead was loaded in silica gel on a single-zone refined Re filament. Both U and Pb were analyzed in single-collector peak-switching mode using a Daly ion-counting system. Data processing and age calculations were completed using the applications Tripoli and U-Pb_Redux developed as part of the EARTHTIME initiative (Bowring et al., 2011). Decay constants used were $^{238}U = 1.55125 \times 10^{-10}\ a^{-1}$ and $^{235}U = 9.8485 \times 10^{-10}\ a^{-1}$ (Steiger and Jäger, 1977).

Mineral Identification

Samples MBL7, SAM 4-8, and HS 6 were powdered and analyzed using a Shimadzu 6000 X-Ray Diffractometer in the Department of Geology at Appalachian State University with a CuKα beam and a set wavelength of 1.524 Å. Thin sections for optical petrography were also prepared using standard polishing methods, and analyzed on petrographic microscopes at Appalachian State University.

Whole Rock Geochemistry

Samples MBL-7, HS-6, HS-7, HS-8A, and HS-8B were all analyzed for major, trace, and rare earth elements. Whole rock geochemical analysis were performed by Activation Laboratories (Ancaster, ON, Canada).

Chapter 5. Results

Petrography

Sample MBL 7 (Figure 5) is a very immature sandstone with very small grain size (<100μ) and poorly sorted, angular grains of plagioclase, quartz, and scattered illite. Optical petrography of MBL 7 indicates that the sample was physically weathered with very little transportation since it has a very small grain size and poorly sorted grains. Sample SAM 4-8 (Figure 6) is a conglomerate consisting of coarse grains (1mm-3mm) with semi-rounded clasts of plagioclase, quartz, and sparse illite. Sample HS 6 (Figure 7) is a porphyritic basalt, with optical petrography revealing an amygdule filled by serpentine and needle-like white mica flakes with surrounding needles of plagioclase and altered pyroxene.

XRD

Both sample MBL 7 (Figure 8) and SAM 4-8 (Figure 9) have a mineralogy consisting of abundant quartz, albite, and sparse illite. Sample HS 6 has a mineralogy consisting of clinopyroxene, calcite, and albite (Figure 10).

Whole Rock Geochemistry

Major, trace, and rare earth elements (Table 2) were plotted on tectonomagmatic discrimination diagrams to identify potential sediment sources (Figure 11). All samples plotted with an arc basalt sediment source (Figure 11).

Geochronology Results

Age calculations for the five separate zircon fractions of samples SAM 4-8 (Table 3) and MBL 7 (Table 4) are denoted by F-(1-5). For sample, SAM 4-8, two fractions (F-4 and F-5) plotted off concordia (Figure 12). Possible reasons for discordance is attributed to Pb loss, U loss, or disequilibrium (Mattinson, 2005), and therefore these two fractions were not considered when calculating the age of the unit. For the other three zircon fractions, dates recorded are 371.79 +/-0.40 Ma (F-1), 397.00+/- 0.47 Ma (F-2), and 375.81 +/- 0.41 (F-3) Ma (Table 3). Fraction F-3 had exceptionally low error associated with its date because of a relatively high radiogenic Pb to common Pb ratio (Pb^*/Pb_c). Weighted mean and average of dates that plot on concordia indicate an age of 375.81 +/- 1.20 Ma, suggesting a Frasnian age.

For sample MBL 7, all five zircon fractions plotted on concordia (Figure 13). Dates recorded are 380.24 +/- 9 Ma (F-1), 380.08 +/- 2.83 Ma (F-2), 376.06 +/- 0.98 Ma (F-3), 382.50+/- 4.74 (F-4), and 376.69 +/- 7.123 Ma (F-5) (Table 4). Fraction F-5 has the highest error, most likely due to its lack of U available in the zircon grain. Fraction F-3 has the lowest error because of its relatively high Pb^*/Pb_c ratio. Weighted mean average from the five zircon fractions of MBL 7 suggest an age of 376.75 +/- 0.90 Ma, also suggesting a Frasnian age.

Chapter 6. Discussion and Conclusions

Both SAM 4-8 and MBL 7 are sedimentary rocks. When considering the relevance of ages from zircons found in sedimentary rocks rather than igneous rocks, it is important to have evidence to suggest the zircons are representative of the rock being dated, rather than an alternate source (Schoene, 2014). Determining the source of the zircons must include one or more of the following scenarios: (1) provenance analysis suggesting a host sediment source, (2) detailed stratigraphy of the field site with particular attention to interbedded lava flows, and (3) paleogeographic reconstructions to infer tectonic environment of the time of sediment deposition.

Provenance analysis via trace element geochemistry indicates an arc basalt sediment source for all samples (Figure 11), consistent with paleogeographic reconstructions of the Central Asian Orogenic Belt (CAOB) region (Figure 1A). In addition, fieldwork in 2014 has revealed the presence of lava flow found in two sections: the Kushuut-Shiveet River Locality (Figure 14), and the Shiveet Mountain Locality (Figure 15).

It is not surprising that the three zircon fractions from SAM 4-8 resulted in different ages, as the rock is a conglomerate. But it is important to take note that the small deviation of calculated age between the zircons suggest that the zircons are from the same source and the final averaged age is representative of the origin of SAM 4-8 rather than other, older rock sources.

Considering the mineralogy, grain size, poor sorting, and angular clasts of sample MBL, MBL 7 is therefore classified as a mafic, immature sandstone that weathered directly from a basalt with little transportation. This assumption is supported when analyzing geochronology results. All fractions of MBL 7 plotted on concordia (therefore all were considered when

finalizing age calculations of MBL 7), and all five fractions resulted in very similar ages (within 4 my of each other) (Table 4), with a final average age of 376.75 +/- 0.90 Ma.

Stratigraphic Implications

Previous fieldwork in western Mongolia in 2012 suggested that the Baruunhuurai Formation and the Samnuuruul Formation contained both the F-F and D-C boundary, respectively (Kido et al., 2013). Additional fieldwork in 2014 by IGCP 596 & 580, however, involved more detailed observations of brachiopods (Bernard Mottequin and Edouard Poty-personal communication, 2014) and corals and suggested these sediments might be Frasnian in age rather than Famennian (Gonchigdorj and Kido, 2015).

The results of radiometric ages of detrital zircons from immature sediments in these sections likewise suggest that the section is Frasnian in age, and that the beds in the Buduun Khargait River section have been overturned. Additional conodont biostratigraphy and palynology is needed to confirm a Frasnian age for these sediments. These results will help identify exactly where the F-F and D-C boundaries can be found within sections in Mongolia, and guide future research into the scope and extent of marine anoxia in the CAOB during Late Devonian mass extinction events.

Tables.

Table 1. Sample list of rocks collected while in Mongolia 2014 with stratigraphic position and rock description. Samples in bold were analyzed for zircon dating.

Sample Number	Stratigraphic Position (cm)	Rock Description
SAM 2/60	5920	Green shale
SAM 2/61	5950	Green shale with calcareous tuff including nodule
SAM 2/64 E	5960	Gray shale
SAM 2/64 F	5960	Sandy silt layer
SAM 2/64 G	5960	Black shale/silt
SAM 2/64 H	5960	Gray shale (weathers greenish)
SAM 2/64 I	59.6	Green/gray shale
SAM 2/66 A	5980	Green/gray shale
SAM 2/66 B	5980	Green/gray shale
SAM 2/66 C	5980	Green/gray shale
SAM 2/66 D	5980	Green/gray shale
SAM 3/1	5990	Dark green shale
SAM 3/2	6000	Green shale
SAM 3/3	6020	Dolomite
SAM 3/16	6390	Weathered siltstone that seems to be derived from a basalt?
SAM 3/17	6400	Dark green siltstone
SAM 3/18	6430	Immature sandstone with angular and arkosic clasts
SAM 3/19	6450	Shale/mudstone-fined grained but blocky
Fish Bowl E	n/a	Fine grained limestone with phosphate nodules
Fish Bowl W	n/a	Fine grained limestone with phosphate nodules
SAM 4/1	6740	Medium grained sandstone
SAM 4/2	6840	Green shale
SAM 4/7	6940	Dark greenish/gray siltstone
SAM 4/8 (finer)	7020	Finer grained sandstone
SAM 4/8 (coarser)	7220	Coarser grained sandstone
SAM 4/10	7500	Conglomerate with crossbedded/finer grained sandstone at the base
SAM 4/13	8000	Coarse grained sandstone grading into coarse conglomerate
SAM 4/14	8100	Coarse conglomerate
SAM 4/15	8200	Dark green siltstone
SAM 4/18	8300	Coarse grained sandstone
SAM 4/19	8400	Coarse grained sandstone
SAM 4/23	8780	Coarse grained sandstone
SAM Mountain 1	n/a	
SAM Mountain 3	n/a	
SAM South Ridge Microbialite	n/a	Microbialite
SAM South Ridge Sandstone	n/a	Coarse grained sandstone
South Ridge Chert Band	n/a	Chert band
South Ridge Black Shale	n/a	Black shale
SAM Stramatolite	n/a	Stramatolite

Sample Number	Stratigraphic Position (cm)	Rock Description
HS 1	-	Fossiliferous sandstone
HS 2	-	Black/red conglomerate
HS 3	-	Coarse cobbled conglomerate
HS 4	-	Mafic sandstone
HS 5	-	Dike basalt layer
HS 6	-	Pillow basalt
HS 7	-	Immature mafic sandstone/crystalline basalt?
HS 8a	-	Black shale
HS 8b	-	Fossiliferous black shale
MBL 7	-	Immature mafic sandstone
MBL 8	-	Sandstone
MBL 9	-	Chilled margin of basalt
MBL 11	-	Sandstone
Lost Canyon Bentonite	-	Bentonite

Table 2. Whole rock geochemistry of samples MBL-7, HS-6, HS-7, HS-8A, and HS-8B.

Analyte Symbol	Unit Symbol	Detection Limit	Analysis Method	MBL-7	HS-6	HS-7	HS-8A	HS-8B
SiO_2	%	0.01	FUS-ICP	76.17	43.26	64.58	71.73	52.43
Al_2O_3	%	0.01	FUS-ICP	11.16	16.86	15.01	12.91	15.33
Fe_2O_3	%	0.01	FUS-ICP	4.24	15.66	7.68	8.16	19.52
MnO	%	0.001	FUS-ICP	0.078	0.203	0.13	0.09	0.353
MgO	%	0.01	FUS-ICP	0.56	2.95	0.74	0.98	2.32
CaO	%	0.01	FUS-ICP	0.65	5.02	1.78	0.26	1.07
Na_2O	%	0.01	FUS-ICP	4.37	4.8	5.53	0.65	0.35
K_2O	%	0.01	FUS-ICP	0.57	0.17	0.19	0.91	0.5
TiO_2	%	0.001	FUS-ICP	0.984	2.344	0.513	0.578	1.01
P_2O_5	%	0.01	FUS-ICP	0.08	0.56	0.02	0.04	0.03
LOI	%		FUS-ICP	1.77	7.42	4.5	4.24	6.09
Au	ppb	1	INAA	< 1	< 1	< 1	< 1	< 1
Ag	ppm	0.5	TD-ICP	< 0.5	< 0.5	< 0.5	< 0.5	< 0.5
As	ppm	1	INAA	9	11	6	3	4
Ba	ppm	1	FUS-ICP	125	148	126	365	176
Be	ppm	1	FUS-ICP	1	1	< 1	1	< 1
Bi	ppm	2	TD-ICP	< 2	< 2	< 2	< 2	3
Br	ppm	0.5	INAA	< 0.5	< 0.5	< 0.5	< 0.5	< 0.5
Cd	ppm	0.5	TD-ICP	< 0.5	< 0.5	< 0.5	< 0.5	< 0.5
Co	ppm	0.1	INAA	10.4	40	10.3	11.4	23.3
Cr	ppm	0.5	INAA	25.3	127	33.7	14.7	49
Cs	ppm	0.2	INAA	< 0.2	< 0.2	< 0.2	0.4	< 0.2
Cu	ppm	1	TD-ICP	13	66	9	28	19
Hf	ppm	0.2	INAA	4	4.4	2.8	4.6	5.4
Hg	ppm	1	INAA	< 1	< 1	< 1	< 1	< 1
Ir	ppb	1	INAA	< 1	< 1	< 1	< 1	< 1
Mo	ppm	2	TD-ICP	< 2	< 2	< 2	< 2	2
Ni	ppm	1	TD-ICP	8	97	6	9	15
Pb	ppm	5	TD-ICP	8	10	< 5	< 5	7
Rb	ppm	10	INAA	< 10	< 10	< 10	< 10	< 10
S	%	0.001	TD-ICP	0.006	0.019	0.006	0.006	0.01
Sb	ppm	0.1	INAA	0.7	0.1	0.4	0.4	0.4
Sc	ppm	0.001	INAA	9.89	17.1	9.2	13.9	18.7
Se	ppm	0.5	INAA	< 0.5	< 0.5	< 0.5	< 0.5	< 0.5
Sr	ppm	2	FUS-ICP	193	276	137	81	52
Ta	ppm	0.3	INAA	< 0.3	< 0.3	< 0.3	< 0.3	< 0.3
Th	ppm	0.1	INAA	6	4.9	1.8	4.1	5.2
U	ppm	5	INAA	0.4	1	0.9	1.1	1.9
V	ppm	1	FUS-ICP	43	191	38	73	187
W	ppm	1	INAA	< 1	< 1	< 1	< 1	< 1
Y	ppm	1	FUS-ICP	36	21	20	20	16
Zn	ppm	2	TD-ICP	42	117	64	98	177
Zr	ppm	2	FUS-ICP	139	178	94	133	198
La	ppm	0.05	INAA	21.4	37.5	16.8	14.5	15.8
Ce	ppm	1	INAA	47	68	32	27	55
Nd	ppm	1	INAA	27	28	14	14	17
Sm	ppm	0.01	INAA	7.12	7.81	3.52	2.61	3.64
Eu	ppm	0.2	INAA	2.3	3.1	1.2	0.6	1.4
Tb	ppm	0.1	INAA	1	1.2	0.6	0.5	0.8
Yb	ppm	0.05	INAA	3.48	1.92	2.25	2.54	3.53
Lu	ppm	0.01	INAA	0.57	0.27	0.39	0.41	0.63

Table 3. Geochronology results for sample SAM 4-8. Fraction F-3 had the lowest associated error, attributed to the high content of radiogenic Pb (Pb*) and the ratio of radiogenic Pb to common Pb (Pb_c).

	F-1	**F-2**	**F-3**	**F-4**	**F-5**
$^{206}Pb/^{238}U$	371.79	397.00	375.81	543.87	274.89
±2σ	0	0.47	0.41	1.06	0.34
$^{207}Pb/^{235}U$	307.40	395.70	374.65	511.40	287.48
±2σ	35.61	2.74	2.55	4.53	2.27
$^{207}Pb/^{206}Pb$	-155.88	388.62	368.07	369.16	391.88
±2σ	346.74	17.41	17.45	23.63	18.71
Corr. coefficient	0	0.55	0.42	0.47	0.62
% discordance	338.45	-2.13	-2.08	-47.30	29.88
Th/U	0.36	0.41	0.44	0.46	0.49
Pb* (pg)	4.10	39.50	24.62	33.78	34.39
Pb_c	1.17	2.056	1.19	2.43	1.86
Pb^*/Pb_c	3.52	19.21	20.73	13.89	18.48
$^{206}Pb/^{204}Pb$	243.60	1219.65	1302.15	876.08	1148.44
$^{206}Pb/^{238}U$	0.06	0.06	0.06	0.09	0.04
±2σ %	0	0.12	0.11	0.20	0.12
$^{207}Pb/^{235}U$	0.35	0.47	0.45	0.65	0.32
±2σ %	13.43	0.83	0.81	1.13	0.91
207Pb/206Pb	0.04	0.05	0.05	0.05	0.05
±2σ %	13.96	0.78	0.77	1.05	0.84
Corr. coefficient	0	0.55	0.42	0.47	0.62

Table 4. Geochronology results of sample MBL 7. Fraction F-3 had the lowest associated error, attributed to the high content of radiogenic Pb (Pb*) and the ratio of radiogenic Pb to common Pb (Pb_c).

	F-1	**F-2**	**F-3**	**F-4**	**F-5**
$^{206}Pb/^{238}U$	380.24	380.08	376.06	382.49	376.69
±2σ	9.18	2.82	0.98	4.74	7.13
$^{207}Pb/^{235}U$	362.54	378.09	370.37	356.46	309.36
±2σ	36.49	32.72	7.24	43.73	102.32
$^{207}Pb/^{206}Pb$	251.31	366.46	335.44	190.80	-171.09
±2σ	253.02	221.57	49.93	318.69	918.33
Corr. coefficient	0.48	0.72	0.53	0.688	0.78
% discordance	-51.27	-3.69	-12.08	-100.42	320.12
Th/U	0.60	0.60	0.64	0.58	0.58
Pb* (pg)	5.64	2.81	6.49	1.53	1.48
Pb_c	2.91	1.82	0.78	1.17	2.88
Pb^*/Pb_c	1.94	1.54	8.33	1.31	0.51
$^{206}Pb/^{204}Pb$	134.48	110.39	509.08	97.18	49.67
$^{206}Pb/^{238}U$	0.061	0.061	0.06	0.06	0.06
±2σ %	2.49	0.76	0.267	1.28	1.95
$^{207}Pb/^{235}U$	0.43	0.45	0.44	0.42	0.36
±2σ %	11.97	10.36	2.33	14.55	38.37
207Pb/206Pb	0.05	0.05	0.05	0.05	0.04
±2σ %	10.99	9.83	2.20	13.70	36.86
Corr. coefficient	0.48	0.72	0.53	0.69	0.79

Figures

Figure 1. Paleogeographic reconstruction of our field site located in the Central Asian Orogenic Belt (CAOB) (Fig. A). Rocks analyzed in this study area are from the East Junggar Arc (Fig. B). Modified from Carmichael et al. (2015).

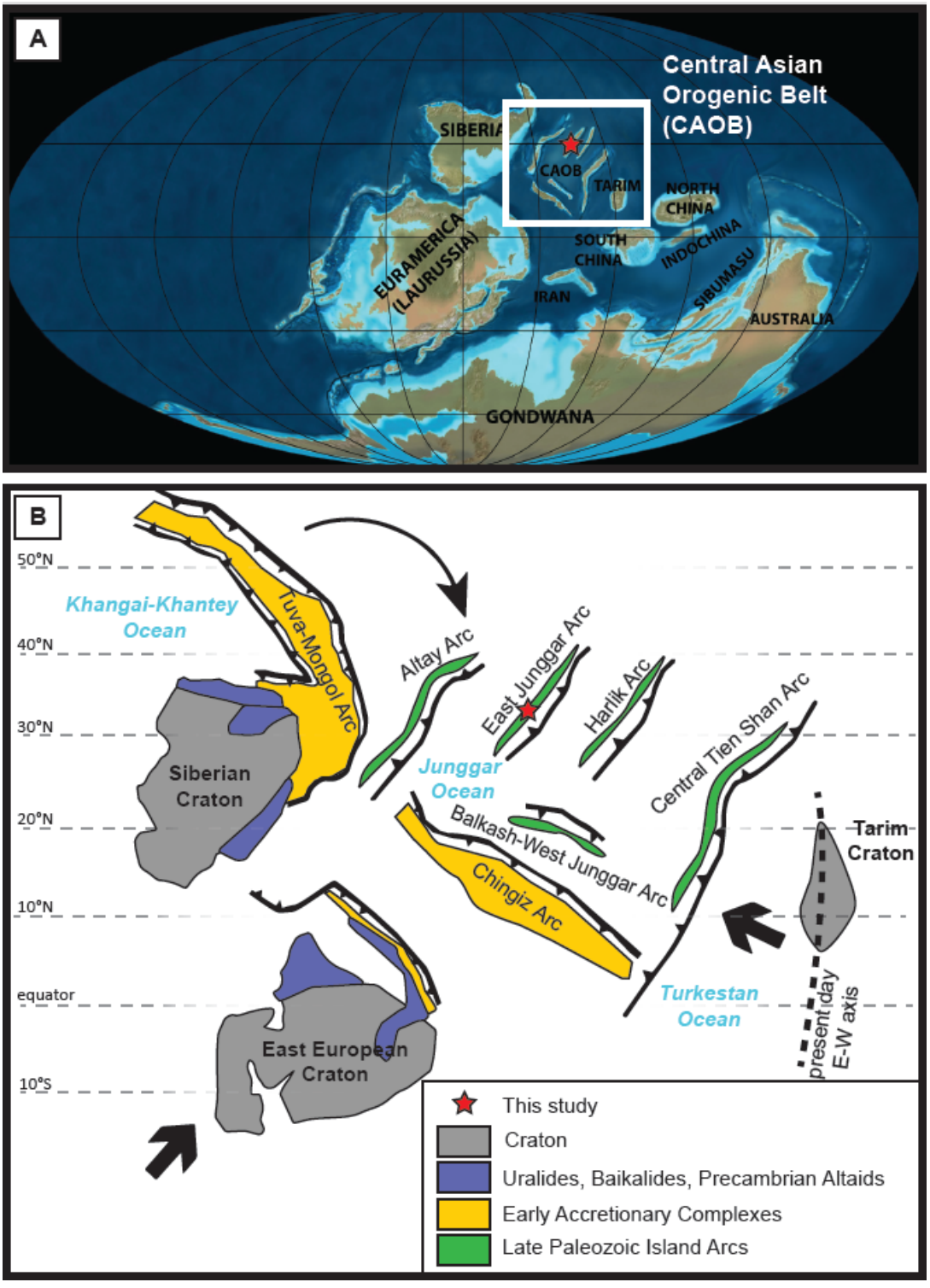

Figure 2. Measured columnar sections of unit 4 of the Sammnuuruul Formation in western Mongolia shown with known biostratigraphy (Kido et al., 2013).

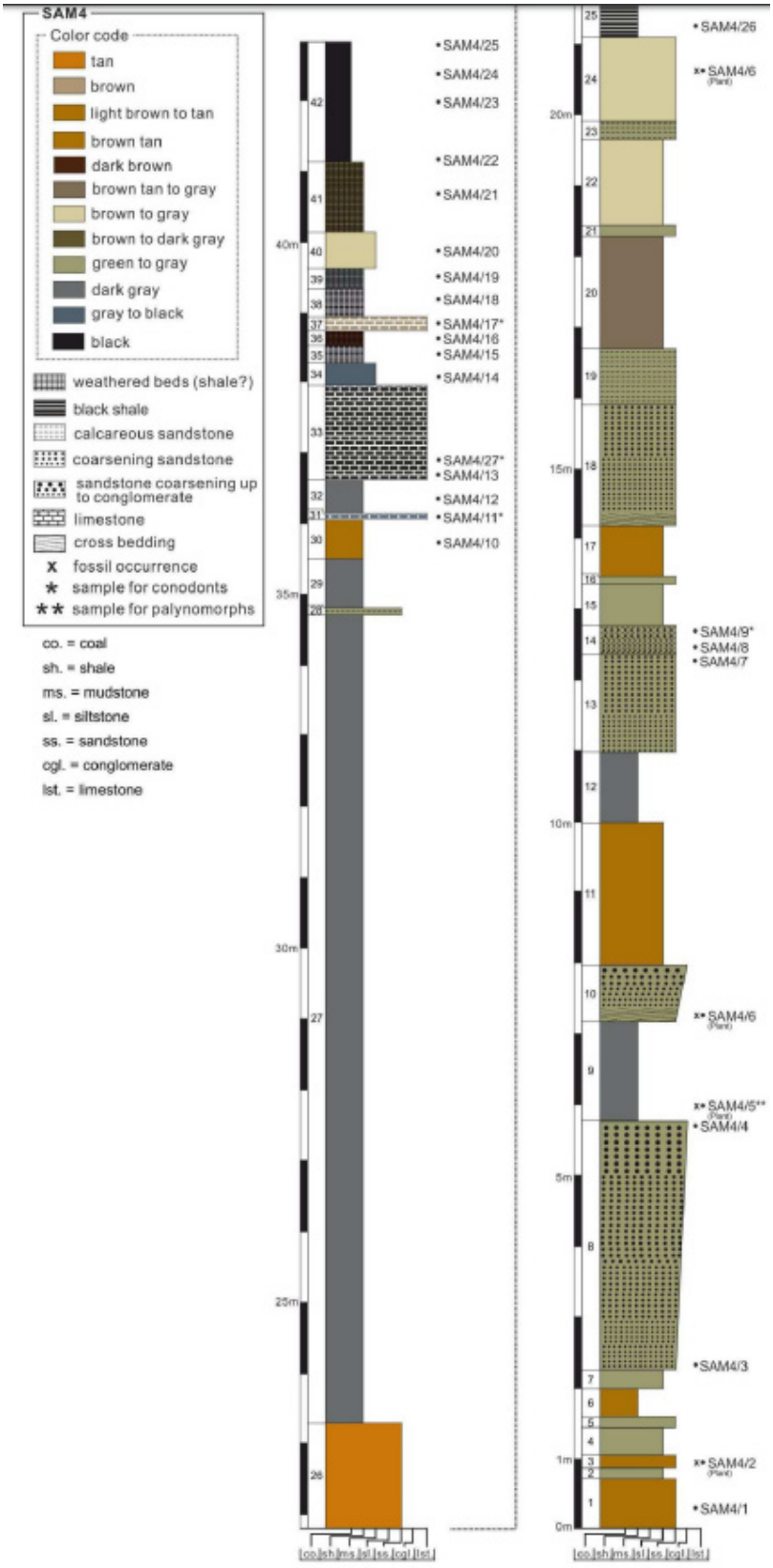

Figure 3. An illustration of the ^{238}U decay chain resulting from successive emission of α- and β-particles. Highlighted in red is the final decay daughter product: stable ^{206}Pb. Once secular equilibrium is achieved, the decay rate of ^{206}Pb is equal to the decay rate of ^{238}U, so one atom of ^{206}Pb is made for every atom of ^{238}U that decays (modified from Schoene, 2014).

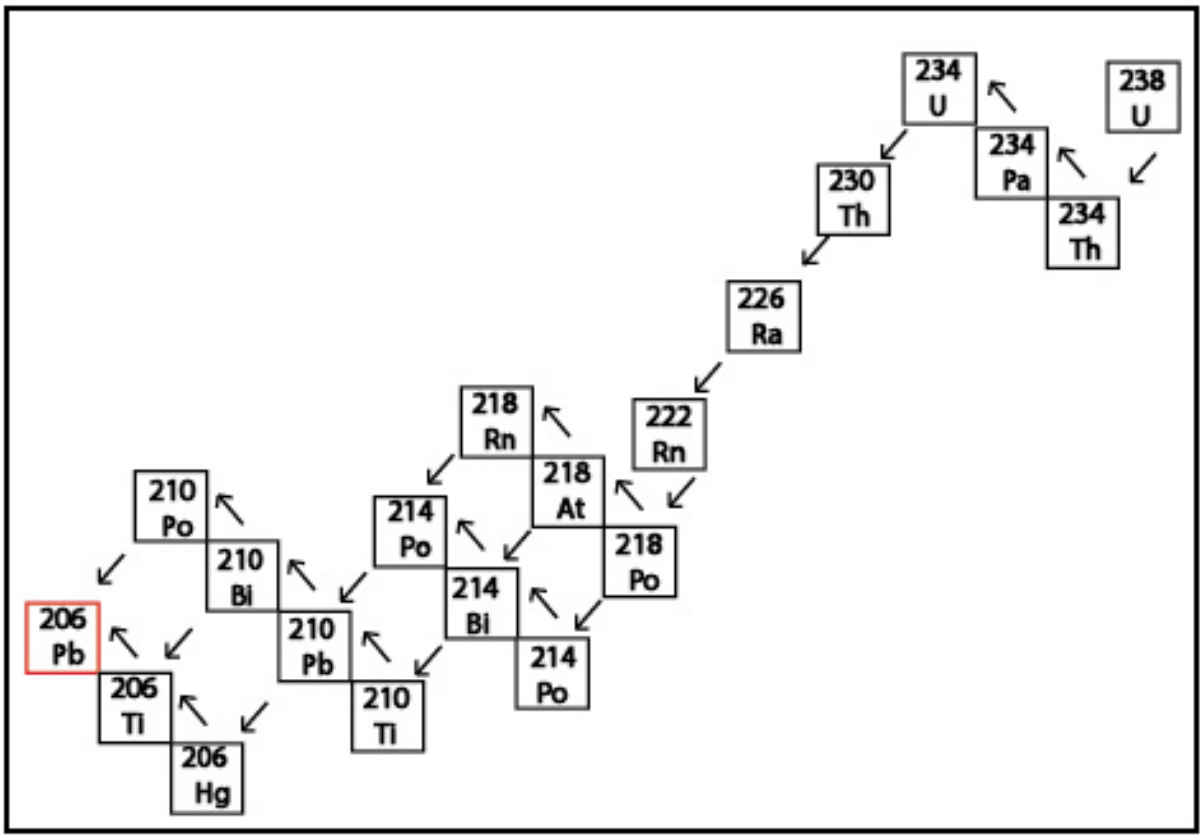

Figure 4. Field map of Mongolia. Locations 3, 4, and 5 correlate with field sites of the Buduun Khargait River, Kushuut-Shiveet River, and Shiveet Mountain Locality (Kido et al., 2013).

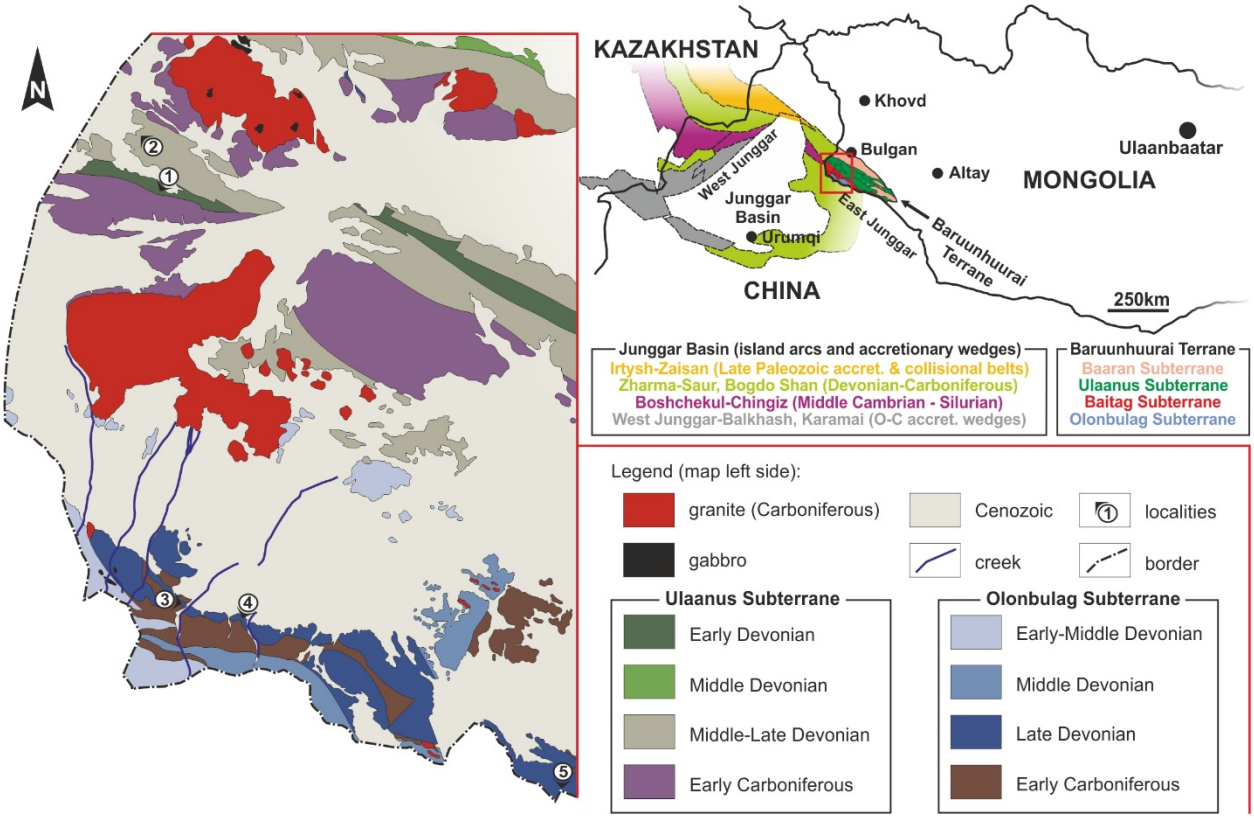

Figure 5. Cross polarized photo of immature mafic sandstone MBL 7. Grains are small in size (<100μ), poorly sorted, and consist of angular grains of plagioclase, quartz, and scattered pyroxene.

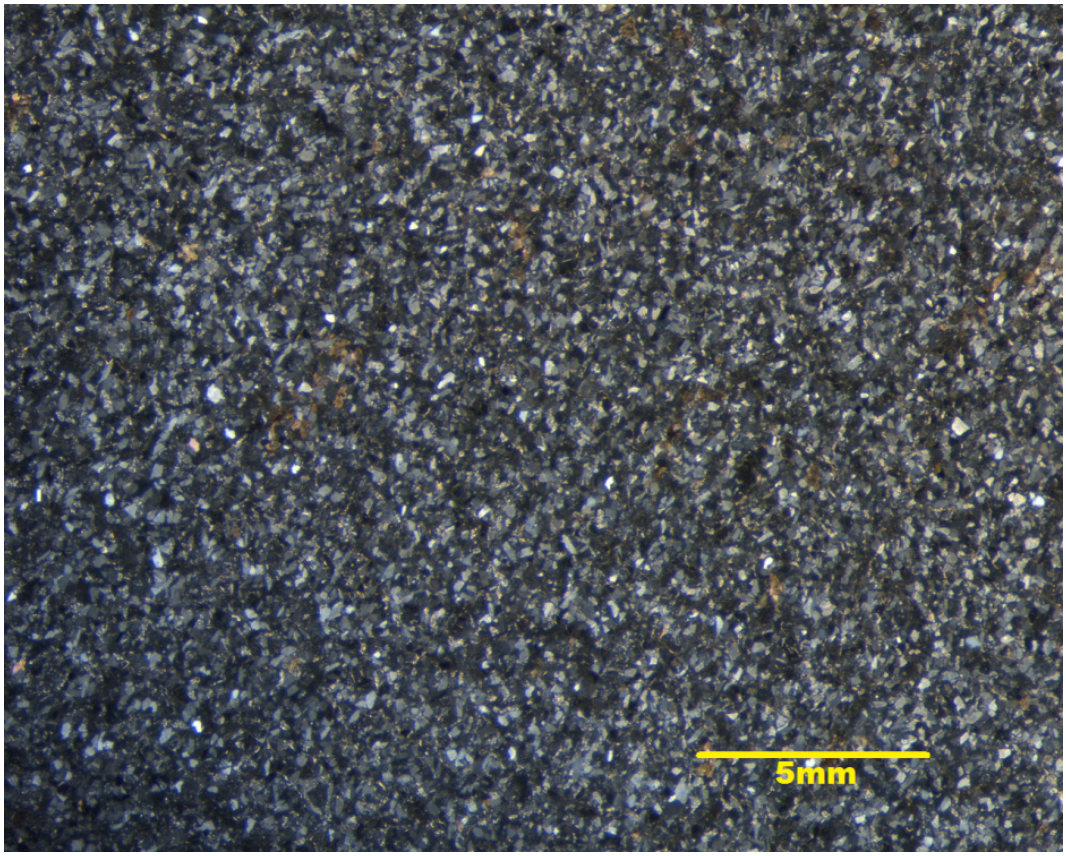

Figure 6. Cross polarized photo of conglomeratic sample SAM 4-8. Grains consist of a coarse grains (1mm-3mm) with semi-rounded clasts of plagioclase, quartz, and sparse hornblende.

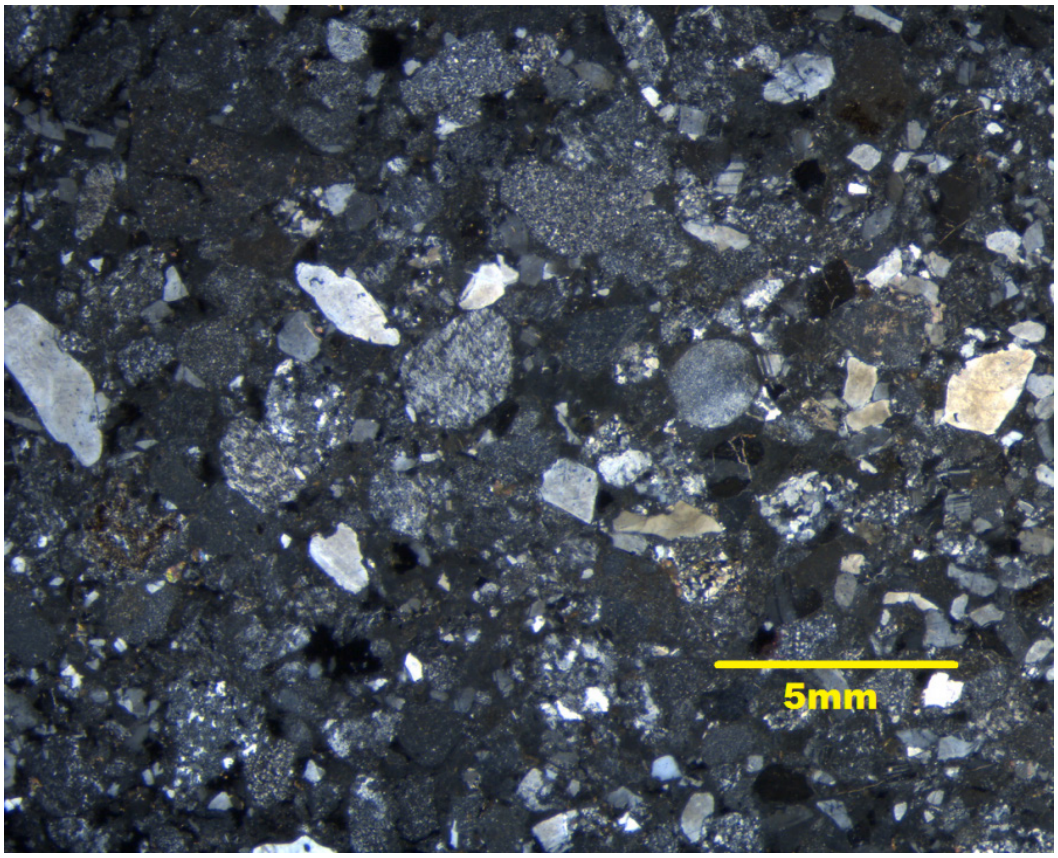

Figure 7. Cross polarized photos of HS 6. Image shows a filled amygdule containing serpentine and needle-like white mica flakes with surrounding plagioclase and altered pyroxene.

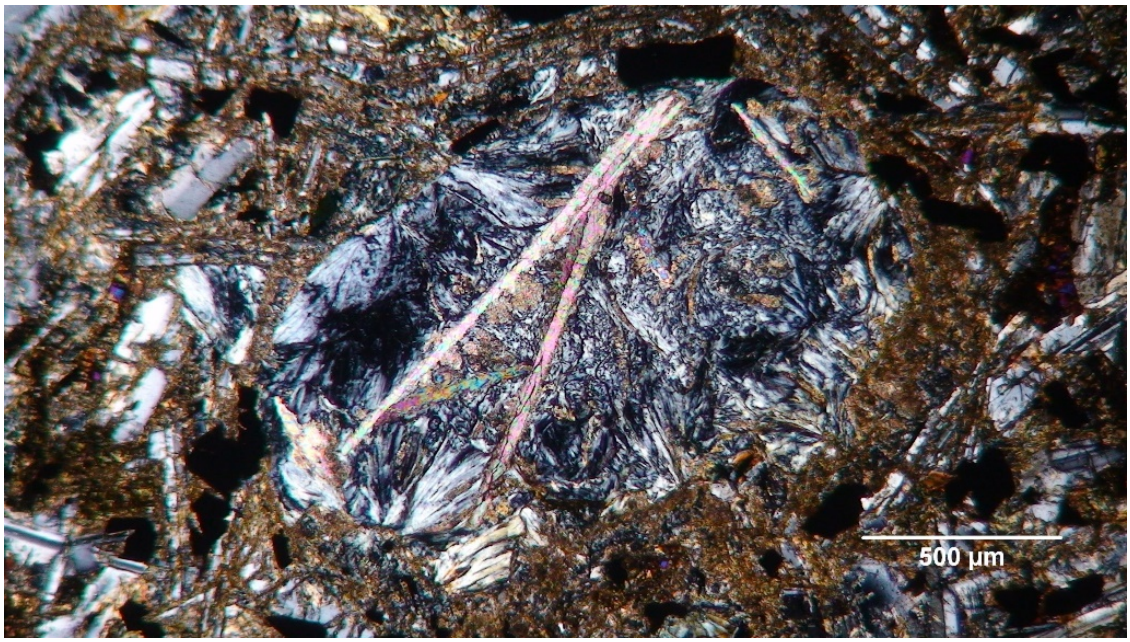

Figure 8. XRD analysis of sample MBL 7. Results show a mineralogy consisting of abundant quartz, albite, and sparse illite.

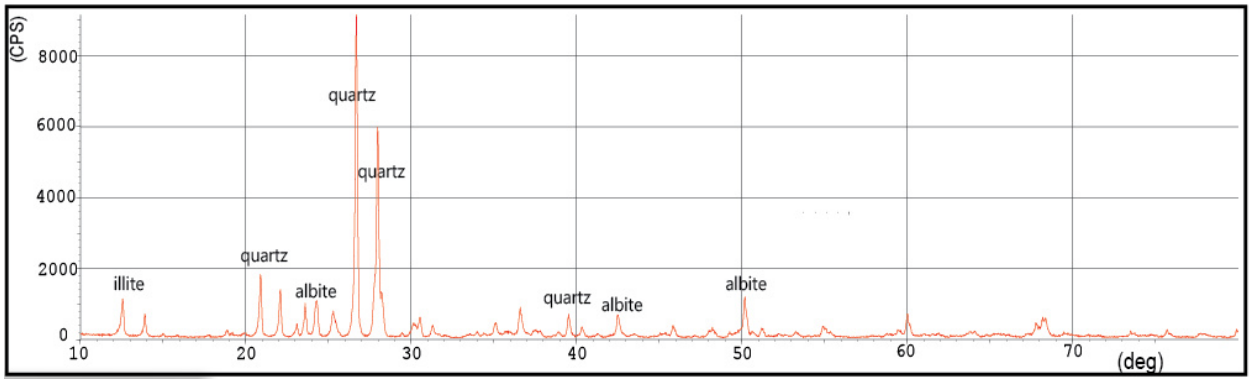

Figure 9. XRD analysis of sample SAM 4-8. Results show a mineralogy consisting of abundant quartz, albite, and sparse illite.

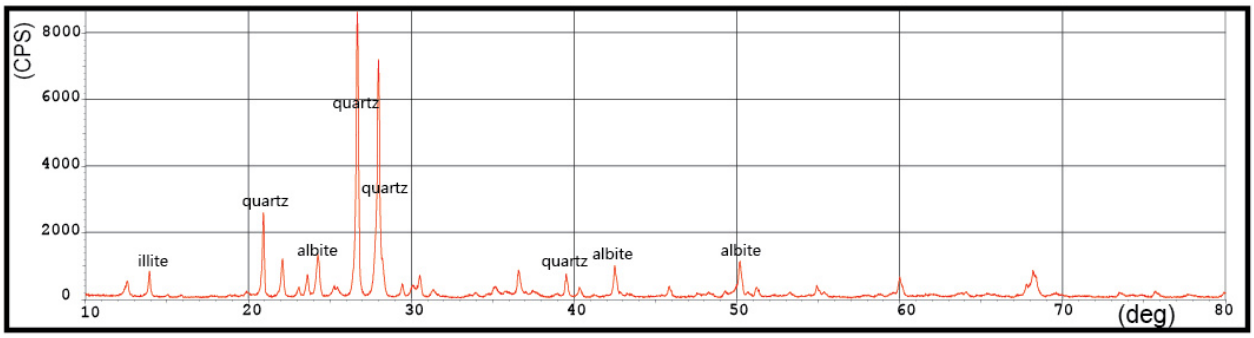

Figure 10. XRD analysis of sample HS 6. Results show a mineralogy consisting of clinopyroxene and albite, with accessory calcite.

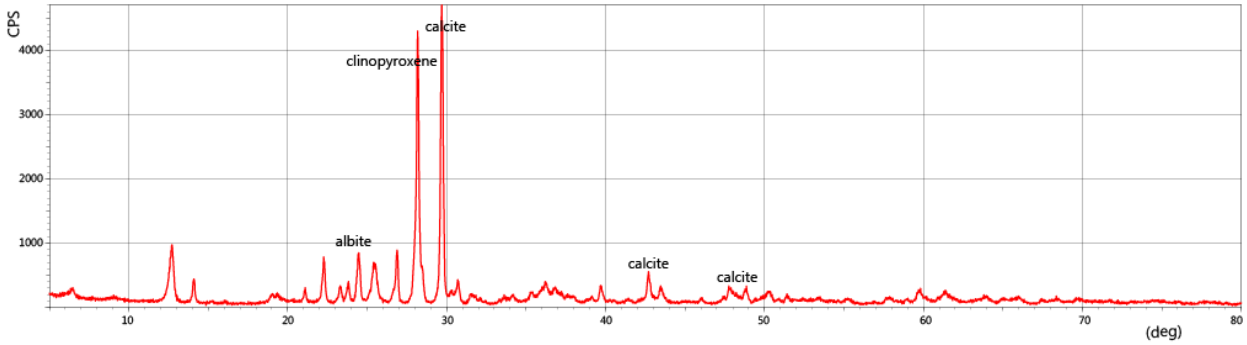

Figure 11. Tectnomagmatic discrimination diagrams with plotted samples including MBL 7, SAM 4-8, and HS 6 (Batchelor et al., 2015). As seen from the diagrams, all samples plot with an arc basalt sediment source from an island arc environment. This suggests that these zircons are from very immature sediments that endured very little transportation, therefore the zircons are representative of the rocks they are found in and not significantly older.

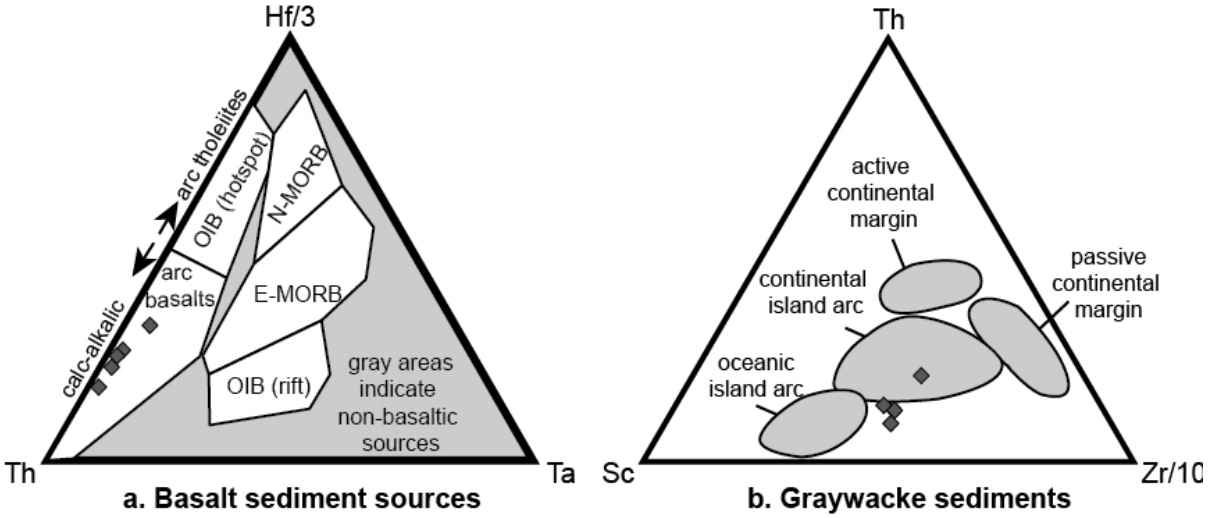

Figure 12. Concordia plot of SAM 4-8 results. Note two of the samples plotted off concordia and are therefore discordant and dates are not taken into consideration when calculating average age (top figure). Fractions F-1 and F-3 had the lowest error (bottom figure).

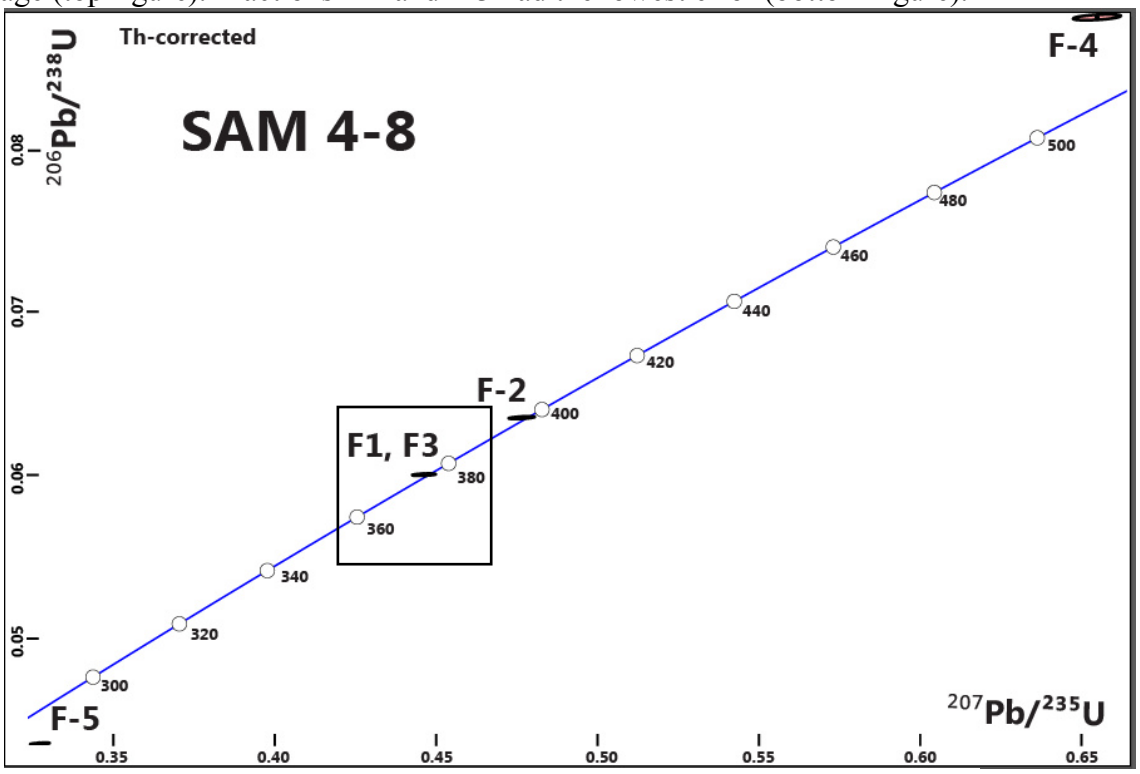

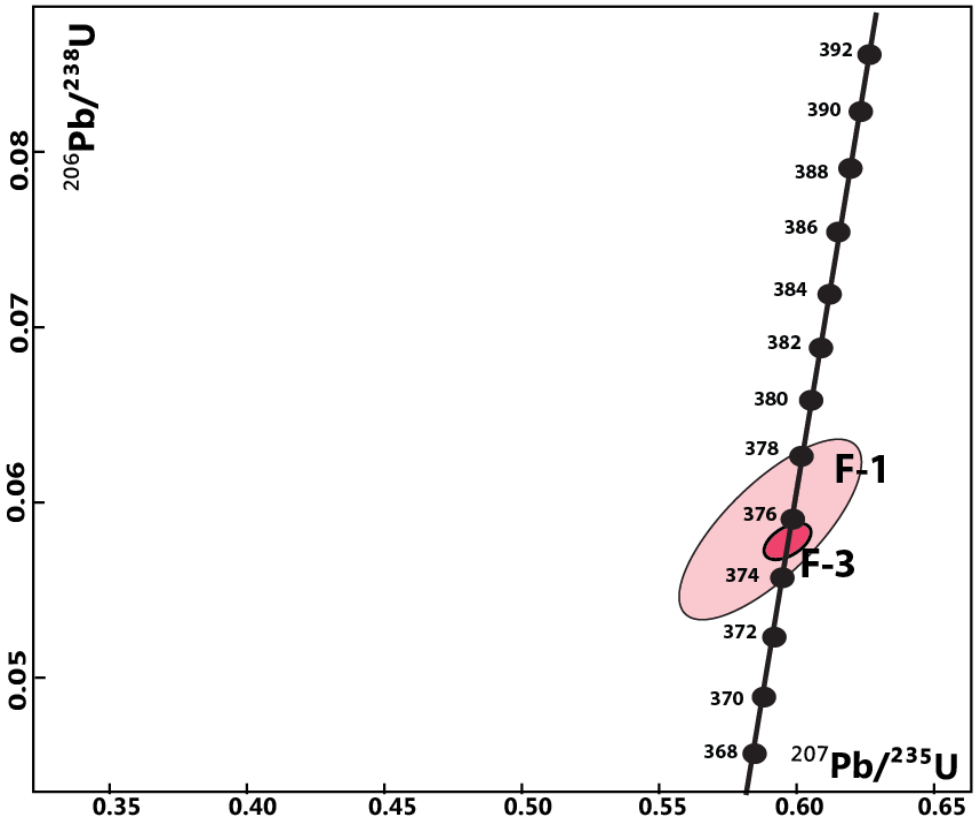

Figure 13. Concordia plot of MBL 7. Samples are clumped together within the same region and all zircon fractions plotted on concordia. Note fraction F-5 (largest circle) is wide like a pancake due to low values of uranium. Fraction F-3 (dark pink circle) gave results with the lowest associated error.

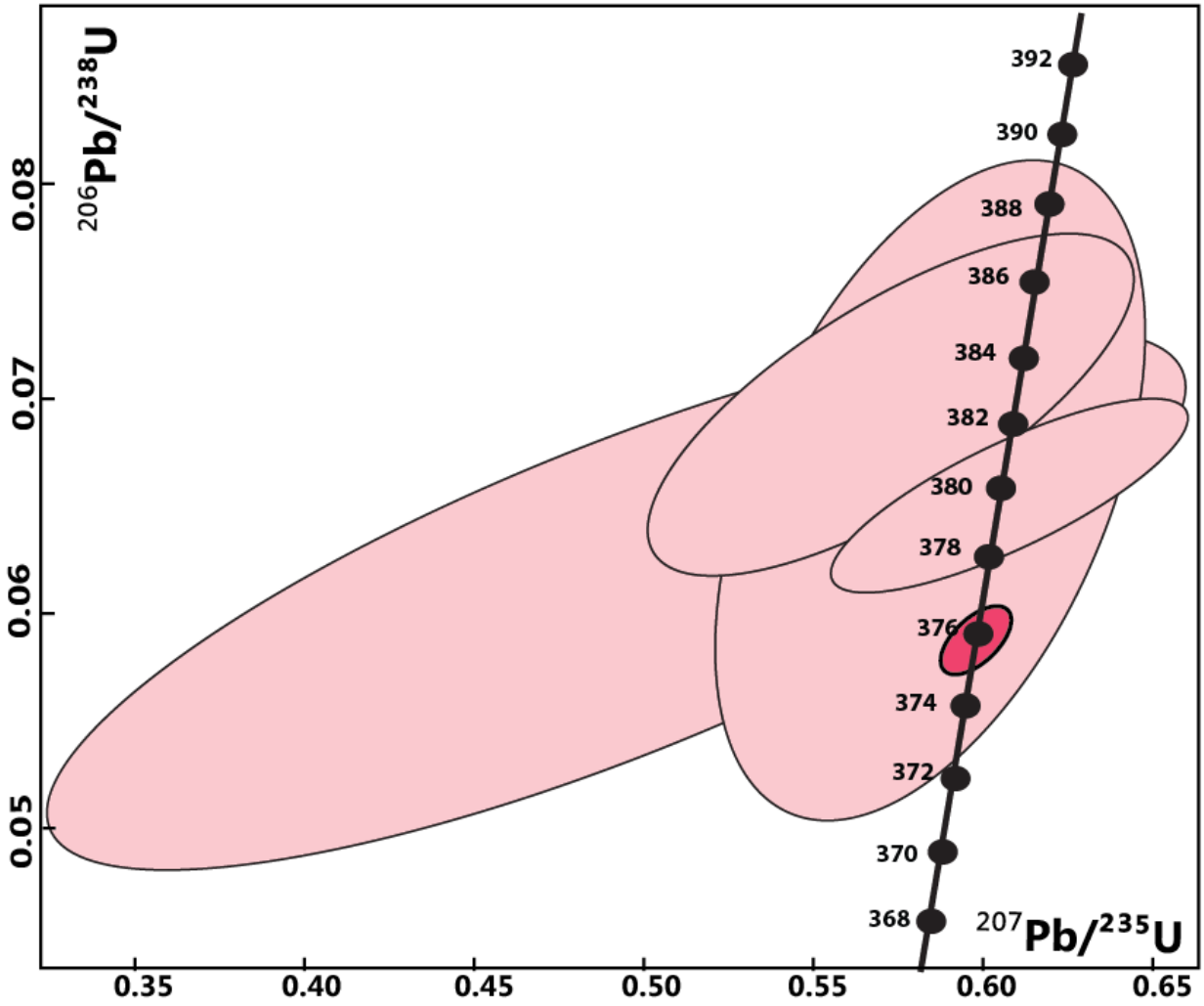

Figure 14. Interbedded lava flows found in the Kushuut-Shiveet River Locality.

Figure 15. Interbedded lava flows found in the Shiveet Mountain Locality.

References

Algeo, T.J., Berner, R.A., Maynard, J.B., Scheckler, S.E., 1995. Late Devonian oceanic anoxic events and biotic crises:"rooted" in the evolution of vascular land plants. GSA today 5, 63-66.

Algeo, T.J., Scheckler, S.E., 1998. Terrestrial-marine teleconnections in the Devonian: links between the evolution of land plants, weathering processes, and marine anoxic events. Philosophical Transactions of the Royal Society B: Biological Sciences 353, 113-130.

Algeo, T.J., Scheckler, S.E., 2010. Land plant evolution and weathering rate changes in the Devonian. Journal of Earth Science 21, 75-78.

Averbuch, O., Tribovillard, N., Devleeschouwer, X., Riquier, L., Mistiaen, B., Vliet-Lanoe, V., 2005. Mountain building-enhanced continental weathering and organic carbon burial as major causes for climatic cooling at the Frasnian–Famennian boundary (c. 376 Ma)? Terra Nova 17, 25-34.

Azmy, K., Poty, E., Brand, U., 2009. High-resolution isotope stratigraphy of the Devonian–Carboniferous boundary in the Namur–Dinant Basin, Belgium. Sedimentary Geology 216, 117-124.

Batchelor, C.J., Carmichael, S.K., Waters, J.A., Coleman, D., Kido, E., Suttner, T.J., 2015. Constraining the ages of Late Devonian extinction events in the Central Asian Orogenic Belt (CAOB): U-Pb zircon ages and igneous petrology, In: Mottequin, B., Denayer, J., Koenigshof, P., Prestianni, C., Olive, S. (Eds.), IGCP596-SDS Symposium. Association STRATA, Brussels, Belgium, pp. 12-13.

Berner, R.A., Kothavala, Z., 2001. GEOCARB III: a revised model of atmospheric CO_2 over Phanerozoic time. American Journal of Science 301, 182-204.

Bond, D., Wignall, P.B., Racki, G., 2004. Extent and duration of marine anoxia during the Frasnian–Famennian (Late Devonian) mass extinction in Poland, Germany, Austria and France. Geological Magazine 141, 173-193.

Bond, D.P., Wignall, P.B., 2014. Large igneous provinces and mass extinctions: an update. Geological Society of America Special Papers 505, SPE505-502.

Bond, D.P., Zatoń, M., Wignall, P.B., Marynowski, L., 2013. Evidence for shallow-water 'Upper Kellwasser'anoxia in the Frasnian–Famennian reefs of Alberta, Canada. Lethaia 46, 355-368.

Bowring, J., McLean, N.M., Bowring, S., 2011. Engineering cyber infrastructure for U-Pb geochronology: Tripoli and U-Pb Redux. Geochemistry, Geophysics, Geosystems 12, doi: 10.1029/2010GC003479.

Brezinski, D.K., Cecil, C.B., Skema, V.W., 2010. Late Devonian glacigenic and associated facies from the central Appalachian Basin, eastern United States. Geological Society of America Bulletin 122, 265-281.

Brezinski, D.K., Cecil, C.B., Skema, V.W., Kertis, C.A., 2009. Evidence for long-term climate change in Upper Devonian strata of the central Appalachians. Palaeogeography, Palaeoclimatology, Palaeoecology 284, 315-325.

Caplan, M.L., Bustin, R.M., 1998. Sedimentology and sequence stratigraphy of Devonian-Carboniferous strata, southern Alberta. Bulletin of Canadian Petroleum Geology 46, 487-514.

Caplan, M.L., Bustin, R.M., 1999. Devonian–Carboniferous Hangenberg mass extinction event, widespread organic-rich mudrock and anoxia: causes and consequences. Palaeogeography, Palaeoclimatology, Palaeoecology 148, 187-207.

Caplan, M.L., Bustin, R.M., Grimm, K.A., 1996. Demise of a Devonian-Carboniferous carbonate ramp by eutrophication. Geology 24, 715-718.

Carmichael, S.K., Waters, J.A., 2015. A decade of deciphering the Late Devonian; more answers, but many more questions In: Mottequin, B., Denayer, J., Koenigshof, P., Prestianni, C., Olive, S. (Eds.), IGCP 596-SDS Symposium. Assocation STRATA, Brussels, Belgium, pp. 27-29.

Carmichael, S.K., Waters, J.A., Batchelor, C.J., Coleman, D.M., Suttner, T.J., Kido, E., Moore, L., Chadimová, L., 2015. Climate instability and tipping points in the Late Devonian: Detection of the Hangenberg Event in an open oceanic island arc in the Central Asian Orogenic Belt. Gondwana Research, doi:10.1016/j.gr.2015.1002.1009.

Carmichael, S.K., Waters, J.A., Suttner, T.J., Kido, E., DeReuil, A.A., 2014. A new model for the Kellwasser Anoxia Events (Late Devonian): Shallow water anoxia in an open oceanic setting in the Central Asian Orogenic Belt. Palaeogeography, Palaeoclimatology, Palaeoecology 399, 394-403.

Chen, D., Wang, J., Racki, G., Li, H., Wang, C., Ma, X., Whalen, M.T., 2013. Large sulphur isotopic perturbations and oceanic changes during the Frasnian–Famennian transition of the Late Devonian. Journal of the Geological Society 170, 465-476.

Choulet, F., Faure, M., Cluzel, D., Chen, Y., Lin, W., Wang, B., Jahn, B.-m., 2012. Architecture and evolution of accretionary orogens in the Altaids collage: The early Paleozoic West Junggar (NW China). American Journal of Science 312, 1098-1145.

Cole, D., Myrow, P., Fike, D., Hakim, A., Gehrels, G., 2015. Uppermost Devonian (Famennian) to Lower Mississippian events of the western US: Stratigraphy, sedimentology, chemostratigraphy, and detrital zircon geochronology. Palaeogeography, Palaeoclimatology, Palaeoecology 427, 1-19.

Cramer, B.D., Saltzman, M.R., Day, J.E., Witzke, B.J., 2008. Record of the Late Devonian Hangenberg global positive carbon-isotope excursion in an epeiric sea setting: carbonate production, organic-carbon burial and paleoceanography during the Late Famennian. Geological Association of Canada 103-118.

De Vleeschouwer, D., Rakociński, M., Racki, G., Bond, D.P., Sobień, K., Claeys, P., 2013. The astronomical rhythm of Late-Devonian climate change (Kowala section, Holy Cross Mountains, Poland). Earth and Planetary Science Letters 365, 25-37.

Faure, G., 1998. Isotope geochronology and its applications to geology. Earth Science Frontiers 5, 17-39.

Formolo, M.J., Riedinger, N., Gill, B.C., 2014. Geochemical evidence for euxinia during the Late Devonian extinction events in the Michigan Basin (USA). Palaeogeography, Palaeoclimatology, Palaeoecology 414, 146-154.

Girard, C., Cornee, J.-J., Corradini, C., Fravalo, A., Feist, R., 2014. Palaeoenvironmental changes at Col des Tribes (Montagne Noire, France), a reference section for the Famennian of north Gondwana-related areas. Geological Magazine 151, 864-884.

Gonchigdorj, S., Kido, E., 2015. Tabulate corals from the Samnuuruul Formation (Upper Devonian) in southwestern Mongolia, In: Mottequin, B., Denayer, J., Koenigshof, P., Prestianni, C., Olive, S. (Eds.), IGCP596-SDS Symposium. Association STRATA, Brussels, Belgium, p. 60.

Isaacson, P.E., Diaz-Martinez, E., Grader, G.W., Kalvoda, J., Babek, O., Devuyst, F.X., 2008. Late Devonian–earliest Mississippian glaciation in Gondwanaland and its biogeographic consequences. Palaeogeography, Palaeoclimatology, Palaeoecology 268, 126-142.

Joachimski, M.M., Buggisch, W., 1993. Anoxic events in the late Frasnian—Causes of the Frasnian-Famennian faunal crisis? Geology 21, 675-678.

Kaiho, K., Yatsu, S., Oba, M., Gorjan, P., Casier, J.-G., Ikeda, M., 2013. A forest fire and soil erosion event during the Late Devonian mass extinction. Palaeogeography, Palaeoclimatology, Palaeoecology 392, 272-280.

Kaiser, S.I., Aretz, M., Becker, R.T., 2015. The global Hangenberg Crisis (Devonian–Carboniferous transition): review of a first-order mass extinction. Geological Society, London, Special Publications 423, doi: 10.1144/SP1423.1149.

Kaiser, S.I., Becker, R.T., Steuber, T., Aboussalam, S.Z., 2011. Climate-controlled mass extinctions, facies, and sea-level changes around the Devonian–Carboniferous boundary in the eastern Anti-Atlas (SE Morocco). Palaeogeography, Palaeoclimatology, Palaeoecology 310, 340-364.

Kido, E., Suttner, T.J., Waters, J.A., Yarinpil, A., Gonchigdorj, S., Atwood, J.W., Webster, G.D., 2013. Devonian deposits of the Baruunhuurai Terrane, western Mongolia (IGCP 596 Field Workshop). Episodes 36, 242-254.

Klug, C., Kroeger, B., Kiessling, W., Mullins, G.L., Servais, T., Fryda, J., Korn, D., Turner, S., 2010. The Devonian nekton revolution. Lethaia 43, 465-477.

Komatsu, T., Kato, S., Hirata, K., Takashima, R., Ogata, Y., Oba, M., Naruse, H., Ta, P.H., Nguyen, P.D., Dang, H.T., 2014. Devonian–Carboniferous transition containing a Hangenberg Black Shale equivalent in the Pho Han Formation on Cat Ba Island, northeastern Vietnam. Palaeogeography, Palaeoclimatology, Palaeoecology 404, 30-43.

Königshof, P., Savage, N., Lutat, P., Sardsud, A., Dopieralska, J., Belka, Z., Racki, G., 2012. Late Devonian sedimentary record of the Paleotethys Ocean–the Mae Sariang section, northwestern Thailand. Journal of Asian Earth Sciences 52, 146-157.

Krogh, T., 1982. Improved accuracy of U-Pb zircon ages by the creation of more concordant systems using an air abrasion technique. Geochimica et Cosmochimica Acta 46, 637-649.

Kumpan, T., Bábek, O., Kalvoda, J., Frýda, J., 2013. Multi-proxy stratigraphic analysis of the Devonian-Carboniferous boundary sections in the Central, Western and Southern Europe: a pathway to the better interregional correlations, In: Hassani El, A., Becker, R.T., Tahiri, A. (Eds.), International Field Symposium-The Late Devonian and Lower Carboniferous of northern Gondwana SDS, Morocco.

Kumpan, T., Bábek, O., Kalvoda, J., Frýda, J., Matys Grygar, T., 2014. A high-resolution, multiproxy stratigraphic analysis of the Devonian–Carboniferous boundary sections in the Moravian Karst (Czech Republic) and a correlation with the Carnic Alps (Austria). Geological Magazine 151, 201-215.

Mattinson, J.M., 2005. Zircon U–Pb chemical abrasion ("CA-TIMS") method: combined annealing and multi-step partial dissolution analysis for improved precision and accuracy of zircon ages. Chemical Geology 220, 47-66.

Matyja, H., Sobien, K., Marynowski, L., Stempień-Sałek, M., Małkowski, K., 2015. The expression of the Hangenberg Event (latest Devonian) in a relatively shallow-marine succession (Pomeranian Basin, Poland): the results of a multi-proxy investigation. Geological Magazine 152, 400-428.

McGhee, G.R., 1996. The late Devonian mass extinction: the Frasnian/Famennian crisis. Columbia University Press. 307 p.

McGhee, G.R., 2013. When the invasion of land failed: the legacy of the Devonian extinctions. Columbia University Press. 360 p.

McGhee, G.R., Clapham, M.E., Sheehan, P.M., Bottjer, D.J., Droser, M.L., 2013. A new ecological-severity ranking of major Phanerozoic biodiversity crises. Palaeogeography, Palaeoclimatology, Palaeoecology 370, 260-270.

McLean, N.M., Bowring, J., Bowring, S., 2011. An algorithm for U-Pb isotope dilution data reduction and uncertainty propagation. Geochemistry, Geophysics, Geosystems 12, doi:10.1029/2010GC003478.

Mottequin, B., Brice, D., Legrand-Blain, M., 2014. Biostratigraphic significance of brachiopods near the Devonian–Carboniferous boundary. Geological Magazine 151, 216-228.

Mundil, R., Ludwig, K.R., Metcalfe, I., Renne, P.R., 2004. Age and timing of the Permian mass extinctions: U/Pb dating of closed-system zircons. Science 305, 1760-1763.

Murphy, A.E., Sageman, B.B., Hollander, D.J., 2000. Eutrophication by decoupling of the marine biogeochemical cycles of C, N, and P: a mechanism for the Late Devonian mass extinction. Geology 28, 427-430.

Myrow, P.M., Ramezani, J., Hanson, A.E., Bowring, S.A., Racki, G., Rakociński, M., 2014. High-precision U–Pb age and duration of the latest Devonian (Famennian) Hangenberg event, and its implications. Terra Nova 26, 222-229.

Nebel, O., Scherer, E.E., Mezger, K., 2011. Evaluation of the 87 Rb decay constant by age comparison against the U–Pb system. Earth and Planetary Science Letters 301, 1-8.

Niedźwiedzki, G., Szrek, P., Narkiewicz, K., Narkiewicz, M., Ahlberg, P.E., 2010. Tetrapod trackways from the early Middle Devonian period of Poland. Nature 463, 43-48.

Perkins, R., Piper, D., Mason, C., 2008. Trace-element budgets in the Ohio/Sunbury shales of Kentucky: constraints on ocean circulation and primary productivity in the Devonian–Mississippian Appalachian Basin. Palaeogeography, Palaeoclimatology, Palaeoecology 265, 14-29.

Racki, G., 2005. Toward understanding Late Devonian global events: few answers, many questions. Developments in Palaeontology and Stratigraphy 20, 5-36.

Rimmer, S.M., 2004. Geochemical paleoredox indicators in Devonian–Mississippian black shales, central Appalachian Basin (USA). Chemical Geology 206, 373-391.

Schindler, E., 1993. Event-stratigraphic markers within the Kellwasser Crisis near the Frasnian/Famennian boundary (Upper Devonian) in Germany. Palaeogeography, Palaeoclimatology, Palaeoecology 104, 115-125.

Schmitz, M.D., Schoene, B., 2007. Derivation of isotope ratios, errors, and error correlations for U-Pb geochronology using ^{205}Pb-^{235}U-(^{233}U)-spiked isotope dilution thermal ionization mass spectrometric data. Geochemistry, Geophysics, Geosystems 8, doi: 10.1029/2006GC001492.

Schoene, B., 2014. U–Th–Pb Geochronology, Treatise on Geochemistry (Second Edition), Elsevier, Oxford. Elsevier Ltd. , Princeton, NJ, pp. 341-378.

Schoene, B., Latkoczy, C., Schaltegger, U., Günther, D., 2010. A new method integrating high-precision U–Pb geochronology with zircon trace element analysis (U–Pb TIMS-TEA). Geochimica et Cosmochimica Acta 74, 7144-7159.

Scotese, C.R., McKerrow, W.S., 1990. Revised world maps and introduction. Geological Society, London, Memoirs 12, 1-21.

Sengör, A., Natal'In, B., Burtman, V., 1993. Evolution of the Altaid tectonic collage and Palaeozoic crustal growth in Eurasia. Nature 364, 299-307.

Sepkoski, J.J., 1986. Global bioevents and the question of periodicity, In: Otto, H.W. (Ed.), Global Bio-Events. Springer, pp. 47-61.

Steiger, R.H., Jäger, E., 1977. Subcommission on geochronology: convention on the use of decay constants in geo-and cosmochronology. Earth and Planetary Science Letters 36, 359-362.

Suttner, T.J., Kido, E., Chen, X., Mawson, R., Waters, J.A., Frýda, J., Mathieson, D., Molloy, P.D., Pickett, J., Webster, G.D., 2014. Stratigraphy and facies development of the marine Late Devonian near the Boulongour Reservoir, northwest Xinjiang, China. Journal of Asian Earth Sciences 80, 101-118.

Wang, K., Geldsetzer, H., Goodfellow, W., Krouse, H., 1996. Carbon and sulfur isotope anomalies across the Frasnian-Famennian extinction boundary, Alberta, Canada. Geology 24, 187-191.

Wetherill, G.W., 1956. Discordant uranium-lead ages. EOS, Transactions American Geophysical Union 37, 320-326.

Xiao, W., Huang, B., Han, C., Sun, S., Li, J., 2010. A review of the western part of the Altaids: a key to understanding the architecture of accretionary orogens. Gondwana Research 18, 253-273.